EES Batteries

PAPER

View Article Online
View Journal

Cite this: DOI: 10.1039/d5eb00098j

In situ construction of multifunctional metaphosphate interphase enabling stable zinc anode with fast Zn^{2+} transport kinetics

Junfeng Wang,†[a] Kaijian Yan,†[b] He Qi,†[a] Dongming Xu,[a] Shaojie Guo,[a] Lihua Pei,[a] Zeya Peng,[a] Dekang Huang,[a] Yanzhu Luo*[a] and Feifei Cao *[a]

Received 28th August 2025,
Accepted 29th October 2025

DOI: 10.1039/d5eb00098j

rsc.li/EESBatteries

Aqueous zinc-ion batteries have significant potential application in large-scale energy storage due to their high safety, affordability, and high energy density. However, serious dendrite growth and side reactions, primarily caused by uneven zinc deposition and direct electrolyte contact, significantly reduce the lifespan of the Zn metal anode. Here, we introduce a multifunctional zinc metaphosphate interphase on ultrahighly oriented Zn with a (002) texture. It is fabricated *in situ* on Zn foil with no boundaries through a straightforward one-step annealing method. The highly conductive zinc metaphosphate interphase is thin with approximately 40 nm thickness. It facilitates rapid Zn-ion transport kinetics and promotes uniform zinc deposition through an epitaxial growth strategy. Additionally, the insulating and stable interphase inhibits corrosion and the hydrogen evolution reaction. As a result of these advantages, the modified Zn foils demonstrate excellent electrochemical performance. In symmetric cells, the zinc metaphosphate interphase-modified Zn anode operates continuously for over 1400 h at an ultrahigh current density of 100 mA cm^{-2} and has an outstanding cycle lifespan of 5900 h at 0.5 mA cm^{-2}. This sustainable protection strategy for the Zn anode lays the foundation to develop high-performance electrodes for aqueous Zn-ion batteries.

Broader context

Aqueous zinc-ion batteries (AZIBs), characterized by intrinsic safety and low cost, are highly desirable for large-scale energy storage. However, the instability of the Zn metal anode, caused by uncontrollable dendrite growth and severe hydrogen evolution reactions, limits their cycle life. To address this issue, we have designed a highly conductive zinc metaphosphate protective interphase with a thickness of ~40 nm and no direct interface with the Zn substrate, enhancing both the cycling stability and high rate capability of AZIBs. As anticipated, this thermal treatment process results in a strongly oriented Zn texture, with the (002) crystal plane predominantly aligned, due to the robust interaction between zinc metaphosphate and the (002) plane. Moreover, symmetric cells exhibit significantly extended cycling life, exceeding 5900 hours at 0.5 mA cm^{-2}, and over 1400 hours at an ultrahigh current density of 100 mA cm^{-2} (more than 16 000 cycles). These results underscore the considerable potential of the zinc metaphosphate interphase for improving the performance of AZIBs. The comprehensive performance of the P–Zn anode represents a significant advancement, demonstrating the potential for developing high-performance Zn-based batteries.

1 Introduction

Rechargeable aqueous Zn-ion batteries (AZIBs) are extensively regarded as the most promising solution for large-scale stationary energy storage systems due to their high theoretical gravimetric and volumetric energy density (820 mAh g^{-1} and 5855 mAh cm^{-3}), low redox potential (−0.76 V *vs.* SHE), high safety, and low cost (approximately ~US$ 2.5 per kg).[1–3] However, two significant obstacles hinder the further implementation of Zn anodes. The primary concern arises from the growth of Zn protrusions/dendrites due to the uneven distribution of the electric field and Zn^{2+} flux, resulting in inferior coulombic efficiency (CE) and a shortened lifespan of AZIBs.[4–6] Moreover, the more negative reduction potential of Zn^{2+}/Zn (−0.76 V *vs.* SHE) compared with H_2O/H_2 (−0.41 V *vs.* SHE) in neutral electrolytes leads to the corrosion of metallic Zn and the hydrogen evolution reaction (HER) at the anode, ultimately reducing the reversibility and stability of active Zn. Thus, suppressing metal dendrites and side reactions is crucial for the practical application of Zn metal anodes.[7–10]

To address the aforementioned issues, regulating the surface state of the Zn metal anode is essential to achieve highly reversible Zn anodes.[11–13] Consequently, various strat-

[a]*College of Chemistry, Huazhong Agricultural University, Wuhan 430070, P. R. China. E-mail: luoyanzhu@mail.hzau.edu.cn, caofeifei@mail.hzau.edu.cn*
[b]*State Key Laboratory of Advanced Technology for Materials Synthesis and Processing, School of Materials Science and Engineering, Wuhan University of Technology, Wuhan 430070, P. R. China*
†These authors contributed equally to this work.

egies have been proposed, such as designing 3D conductive hosts, alloying Zn, preferentially orienting along specific crystal planes, and constructing interfacial protection layers, among others.[14–16] The deposited Zn flakes along the (002) plane have a slight angle of approximately 0°–30° with the substrate, which facilitates uniform Zn metal deposition. Thus, constructing Zn electrodes with a higher exposure of this preferred plane is regarded as an effective strategy to promote planar and dendrite-free Zn deposition. Additionally, owing to the higher free energy of H adsorption on the Zn (002) plane, it effectively inhibits side reactions.[17–20] For instance, an accumulative roll bonding methodology has been developed to fabricate Zn foil with a robust (002) texture, which steadily increases and ultimately reaches ~90% saturation after 12 cycles.[21] However, most strategies are complicated and unable to realize the sole crystallographic orientation of Zn along the (002) plane, and there are still very few reports on the fabrication of single (002)-textured Zn.[22] These findings indicate a crucial need to control the crystal texture of Zn, minimizing other facets like (101), (100), and (102), while also simplifying and enhancing the effectiveness of the preparation procedure.

Additionally, the formation of a stable and robust interphase layer is critical for mitigating dendritic growth and improving the interfacial stability of the Zn anode.[23–25] Interphase layers on Zn anodes are typically classified as either *in situ* formed, *via* electrolyte decomposition during cycling, or artificially constructed before cell assembly. *In situ* interphase layers – such as those composed of ZnF_2 or ZnS – have been widely reported.[26,27] The *in situ* interphase layers are simple to form and naturally compatible with Zn. However, they often suffer from uncontrollable thickness, inhomogeneity, and poor mechanical durability under high current densities. In contrast, artificial interphase layers offer a more tunable and compositionally flexible strategy to design interfacial layers with well-defined structures, thicknesses, and functional properties. Among the reported artificial interphase layers, insoluble $Zn_3(PO_4)_2{\cdot}4H_2O$ has emerged as a highly promising candidate for interfacial protection layers in AZIBs in recent years.[28,29] All of these studies demonstrate that $Zn_3(PO_4)_2$ exhibits lower desolvation activation energy and inhibits dendrites and corrosion. Nevertheless, the low ionic conductivity of $Zn_3(PO_4)_2$ (7.2×10^{-3} mS cm^{-1}) restricts the anode operation to low current densities (<5 mA cm^{-2}). Unlike the isolated tetrahedral structure in $Zn_3(PO_4)_2$, $Zn(PO_3)_2$ features a substructure formed by two bridging oxygen atoms between phosphorus–oxygen tetrahedra. The anionic network forming the metaphosphate chain is able to offer sufficient sites for promoted Zn-ion adsorption, and the created large void spaces could provide favorable channels or interstitial positions for cation diffusion through the structure, thereby facilitating continuous cation transport.[30] Our previous work suggested that the high zincophilic property of the Zn surface could serve as an ion pump to accelerate Zn^{2+} transport in the electrolyte,[31] and the thin interphase layer and good adhesion to the Zn substrate can also significantly improve the batteries' electrochemical performance, especially the fast and continuous ion transport behavior, as well as the durability of Zn.

Based on this motivation, we embarked on exploring a simple and economic approach to design a highly conductive $Zn(PO_3)_2$ protective interphase with a low thickness and no interface with the Zn substrate to promote both the cycling stability and the high rate capability of AZIBs. Here, we report a straightforward one-step annealing method to fabricate a $Zn(PO_3)_2$ interphase directly rooted on the Zn substrate. As expected, a strongly oriented textured Zn with only the (002) crystal plane is achieved in this thermal treatment process due to the robust interaction between $Zn(PO_3)_2$ and the (002) crystal plane. The solid electrolyte interphase layer exhibits no interface with the substrate, thereby delivering remarkable properties for rapid Zn^{2+} transport and effectively promoting uniform and dendrite-free Zn deposition behavior. Consequently, symmetric cells demonstrate extended cycling life exceeding 1400 h at an ultrahigh current density of 100 mA cm^{-2} and 5900 h at 0.5 mA cm^{-2}. These features highlight the significant application potential of the $Zn(PO_3)_2$ interphase in AZIBs.

2 Results and discussion

A thin zinc metaphosphate interphase (referred to as P–Zn) is grown *in situ* on commercial Zn foil through a simple one-step annealing process using $NaH_2PO_4{\cdot}2H_2O$ as the phosphorus source, facilitating scalability for practical applications (Fig. S1 and S2). During annealing at 390 °C under an Ar atmosphere, the decomposition of $NaH_2PO_4{\cdot}2H_2O$ released reactive phosphorus species that reacted with the Zn surface to form a conformal zinc metaphosphate interphase layer. Simultaneously, the high-temperature phosphorus-rich environment promoted surface energy-driven recrystallization and atomic diffusion, leading to the preferential exposure of the Zn (002) crystal plane, known to possess the lowest surface energy in the hexagonal close-packed Zn lattice. As illustrated in the AFM image (Fig. S3), bare Zn exhibits noticeable scratches. They likely originate from the sanding procedure during preparation, which can result in uneven Zn deposition. Following the *in situ* phosphating process, SEM images clearly show that the surface of the P–Zn foil is uniform (Fig. 1a), with the original scratches obscured by numerous generated nanoparticles (Fig. 1b), promoting uniform Zn nucleation and deposition behaviour. The significantly reduced contact angle also indicates an alteration in the morphological and chemical characteristics of P–Zn because the newly generated nanograins effectively regulate the contact behaviour between the electrolyte and P–Zn foil. The outcome is greatly improved wettability of the Zn anode and the electrolyte (Fig. S4). X-ray diffraction (XRD) analysis was further conducted to investigate the crystal structure and composition of the Zn electrodes (Fig. 1c). Interestingly, compared with the original Zn foil, an exceptional crystallographic orientation of Zn along the (002) lattice plane has been exhibited in the XRD pattern of P–Zn, implying

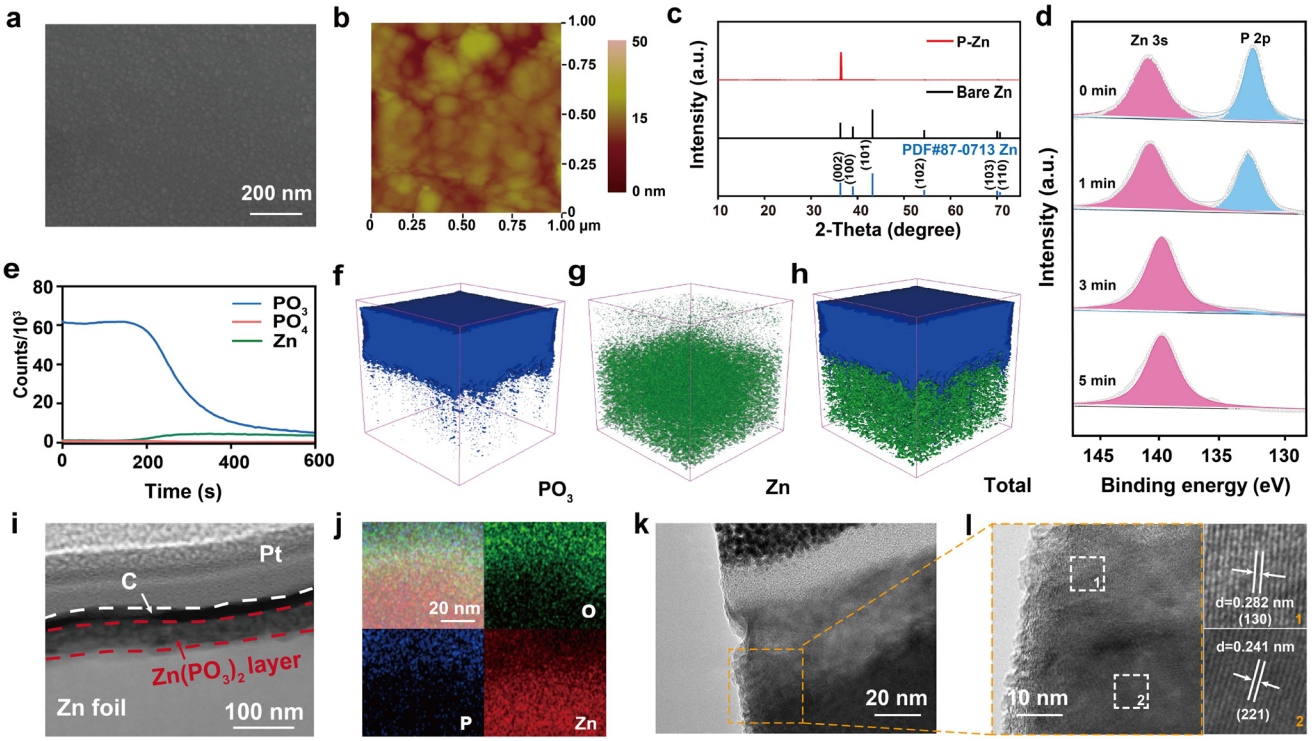

Fig. 1 (a) Top-view SEM image of P–Zn foil. (b) AFM image of the P–Zn surface. (c) XRD patterns of P–Zn foil. (d) XPS depth analysis of P 2p and Zn 3s in P–Zn foil. (e–h) Profiles and spatial distributions of P and Zn elements on P–Zn foil detected by TOF-SIMS. (i) HAADF-STEM image of the P–Zn interphase and (j) the corresponding elemental mappings. (k and l) HRTEM images of selected areas of P–Zn foil.

that atomic rearrangement during annealing promotes texture formation. The absence of a detectable interphase in the XRD pattern may be attributed to its 40 nm thin nature and nanoscale grain size.[32] However, without the assistance of a phosphorus source, the Zn (002) orientation is not as strong as that of P–Zn (Fig. S5). These experimental results confirm the synergistic effect of thermal annealing and the phosphorus source in transforming Zn into a crystal facet with minimal surface energy, as the metal atoms exhibit high mobility and migration capability at high temperature.[33]

The composition of the formed interphase was also analyzed by X-ray photoelectron spectroscopy (XPS) coupled with Ar^+ sputtering. In the P 2p spectra (Fig. 1d), P–Zn shows a signal at 133.5 eV, indicating the presence of P–O bonds. With ongoing Ar^+ sputtering, the intensity of the P elements gradually diminishes, becoming minimal after 3 min and completely disappearing after 5 min. The peaks at 133.5 eV correspond to the presence of P^{5+}, indicating that zinc metaphosphate is the dominant component on the surface.[34] Conversely, the signal of Zn 3s increases with sputtering depth, shifting from 140.2 eV to 139.3 eV after 3 min of sputtering. This finding indicates a reduction in valence from Zn^{2+} in zinc metaphosphate to metallic zinc, which is also confirmed by the Zn 2p spectra (Fig. S6).

Time-of-flight secondary-ion mass spectrometry (TOF-SIMS) was conducted to investigate the spatial distribution and chemical composition of the P–Zn layer. The interphase products including PO_3 and Zn species are observed on the surface of P–Zn. The content remains stable during the initial 180 s of sputtering, with the signal of PO_3 decreasing rapidly while the spatial distribution of Zn increases (Fig. 1e), and the signal of PO_4 is negligible compared to PO_3, suggesting the existence of the $Zn(PO_3)_2$ composite in the interphase layer. The 3D distribution of P and Zn elements confirms the close integration and absence of an interface between the interphase and substrate (Fig. 1f–h). The uniformity and thickness of the interphase layer are further investigated using high-angle annular dark-field scanning transmission electron microscopy (HAADF-STEM) imaging through a standard focused-ion beam lift-out procedure (Fig. 1i and Fig. S7). Analysis of the sample's cross-sectional view clearly shows that the newly generated interphase is densely and uniformly distributed on the surface of Zn foil. It has an average thickness of 40 nm, the thinnest reported for an artificial interphase layer in the literature to our knowledge (Fig. S8). This thin layer effectively shortens ion-diffusion paths and facilitates the rapid transport of Zn^{2+}. Additionally, the formed interphase penetrates the Zn substrate without boundaries. The *in situ* formed interphase significantly enhances contact with the Zn substrate, enhancing the stability of the Zn anode during cycling. Furthermore, elemental mappings indicate that the interphase layer is composed of O, P, and Zn, and $Zn(PO_3)_2$ is located on top of metallic Zn (Fig. 1j). This finding is also confirmed by the line-scan elemental mappings because the signals of P and O elements

in the surface region are definitely higher than those in the inner region (Fig. S9). The lattice fringes of 0.241 and 0.282 nm shown in the HRTEM images can also be well assigned to the (221) and (130) crystal planes of $Zn(PO_3)_2$ (Fig. 1k and l). The HRTEM image of the interphase powder scraped from the surface of P–Zn also manifests the existence of (−221) crystal planes of $Zn(PO_3)_2$ (Fig. S10), reconfirming the $Zn(PO_3)_2$ phase of the interphase layer. The strong orientation of P–Zn along the (002) plane is further confirmed by HRTEM (Fig. S11), which is consistent with the XRD result. Numerous clear parallel lattice fringes with 0.25 nm distance are evident in the region below the $Zn(PO_3)_2$ layer, which correspond to the Zn (002) plane.

Constructing an interfacial protection layer requires good electronic insulation and ionic conductivity, which are essential for developing dendrite-free and high-performance zinc anodes. Four-point resistance measurements were conducted to assess resistivity, revealing that the resistivity of the P–Zn anode is 6.52 μΩ cm, higher than that of bare Zn (5.63 μΩ cm; Fig. S12). The $Zn(PO_3)_2$ interphase, characterized by good electronic insulation, facilitates Zn deposition beneath the passivation layer, preventing direct contact with the electrolyte and thereby inhibiting side reactions. Ionic conductivity, as a crucial aspect of the interphase, is also essential for achieving high-performance zinc anodes. The ionic conductivity of the $Zn(PO_3)_2$ interphase was determined by impedance spectroscopy, revealing a high conductivity of 32.3 mS cm^{-1}. This value is an improvement of several orders of magnitude compared with other reported interphase layers, especially the $Zn_3(PO_4)_2$ interphase (Fig. 2a).[29,30,34–36]

To assess the impact of the $Zn(PO_3)_2$ interphase on Zn plating/stripping behavior, we assembled and tested Zn||Cu half-cells using bare Zn and P–Zn foils as working electrodes, which were tested at a current density of 10.0 mA cm^{-2}. The CE of Zn||Cu half-cells based on the bare Zn foils suddenly decreases due to Zn dendrite growth after 160 cycles. Using P–Zn foils as working electrodes, the cells quickly increase the CE to 99.7% and remain stable over 1500 cycles (Fig. 2b). The nucleation overpotential of the P–Zn||Cu half-cell is 156 mV, whereas that of bare Zn||Cu is 132 mV (Fig. S13). A higher nucleation overpotential results in finer-grained Zn deposition with a favorable crystallographic orientation, thereby inhibiting dendrite growth. Electrochemical impedance spectroscopy of the symmetric cells was conducted to compare the electrochemical performance between bare Zn and P–Zn anodes. Given the insulating properties of the metaphosphate interphase, the impedance of the P–Zn symmetric cell before cycling is slightly higher than that of bare Zn (Fig. S14). After 100 cycles at 1 mA cm^{-2} and 1 mAh cm^{-2}, the impedance of the P–Zn symmetric cell is lower than that of the bare Zn symmetric cell (Fig. 2c). Rapid charge-transfer kinetics are beneficial for the swift transport of Zn^{2+} ions and the long-term stability of the electrode. Fig. 2d illustrates the rate performance of symmetric cells at current densities ranging within 1–100 mA cm^{-2}, maintaining a fixed capacity of 1.0 mAh cm^{-2}. Bare Zn symmetric cells experience severe short circuits at 100 mA cm^{-2} during testing. Conversely, P–Zn symmetric cells demonstrate significantly less voltage hysteresis and maintain stable voltage profiles, even at an ultrahigh current density of 100 mA cm^{-2}. Moreover, they continue to operate as the current density returns to 1 mA cm^{-2}. The depth of discharge is also crucial to the practical application of Zn anodes. Even under harsh conditions with an 88.1% depth of discharge (20 μm Zn foil), the P–Zn electrode maintained stable cycling for 320 h (Fig. 2e). The ion-transport rate is a limiting factor for electrodeposition under high-rate conditions. Remarkably, P–Zn symmetric cells exhibit stable cycling over 1400 h (approximately 16 000 cycles) at an ultra-high current density of 100 mA cm^{-2}, demonstrating excellent rate performance (Fig. 2f). The P–Zn symmetric cells achieve an ultrahigh cumulative capacity of over 16 Ah cm^{-2}, surpassing that of most materials reported in the literature (Fig. 2g).[5,37–43] Accelerated Zn^{2+} migration and a homogenized interfacial Zn^{2+} distribution also contribute to a significantly prolonged cycling life (>5900 h) of P–Zn symmetric cells at 0.5 mA cm^{-2} and 0.5 mAh cm^{-2}, nearly seven times longer than that of bare Zn cells (Fig. 2h). The stable $Zn(PO_3)_2$ interphase layer also effectively prevents continuous electrolyte consumption and inhibits zinc dendrite growth during cycling, resulting in excellent cycling stability at various current densities (Fig. S15).

Deposition behavior is the key factor affecting the electrochemical performance of the Zn anode. To illustrate the regulatory effect of the P–Zn layer, SEM was used to investigate the morphological evolution of Zn anodes with deposition capacities of 1, 5, and 10 mAh cm^{-2}. The poor wettability and zincophilicity of bare Zn lead to an uneven Zn^{2+} flux over the electrode surface, resulting in the formation of scattered spot-shaped deposits (Fig. 3a). As the deposition capacity increases, the electrode surface becomes covered with porous and loose Zn, along with byproducts (Fig. 3b). Eventually, dense upright hexagonal Zn flakes form on the bare Zn anode, posing a risk of short circuits (Fig. 3c). Therefore, the P–Zn electrode exhibits a flat and compact surface across all deposition capacities (Fig. 3d–f). The high diffraction intensity of the (101) plane of the bare Zn anode indicates that Zn^{2+} tends to deposit in the vertical direction. Conversely, the Zn (002) plane of P–Zn consistently dominates among all planes, and even under a deposition of 10 mAh cm^{-2}, the ratio of intensity of the (002) plane to the (101) plane is 38.2 (Fig. 3g). The (002) crystal face of Zn has minimal surface energy, promoting parallel Zn growth on the electrode plane rather than vertical growth, thereby significantly inhibiting dendrite formation. Additionally, *in situ* optical microscopy was conducted to monitor Zn deposition behavior. After 15 min, numerous protrusions appear on bare Zn, evolving into a mossy and rough surface (Fig. 3h). The tip effect increases the charge density at prominent areas, exacerbating Zn dendrite formation and reducing the cycling life of AZIBs. In contrast, the P–Zn electrode exhibits relatively homogeneous deposition without visible dendrites throughout the process (Fig. 3i). To better understand Zn plating/stripping features during cycling, the morphologies of bare Zn and P–Zn electrodes were investigated after varying numbers of cycles.

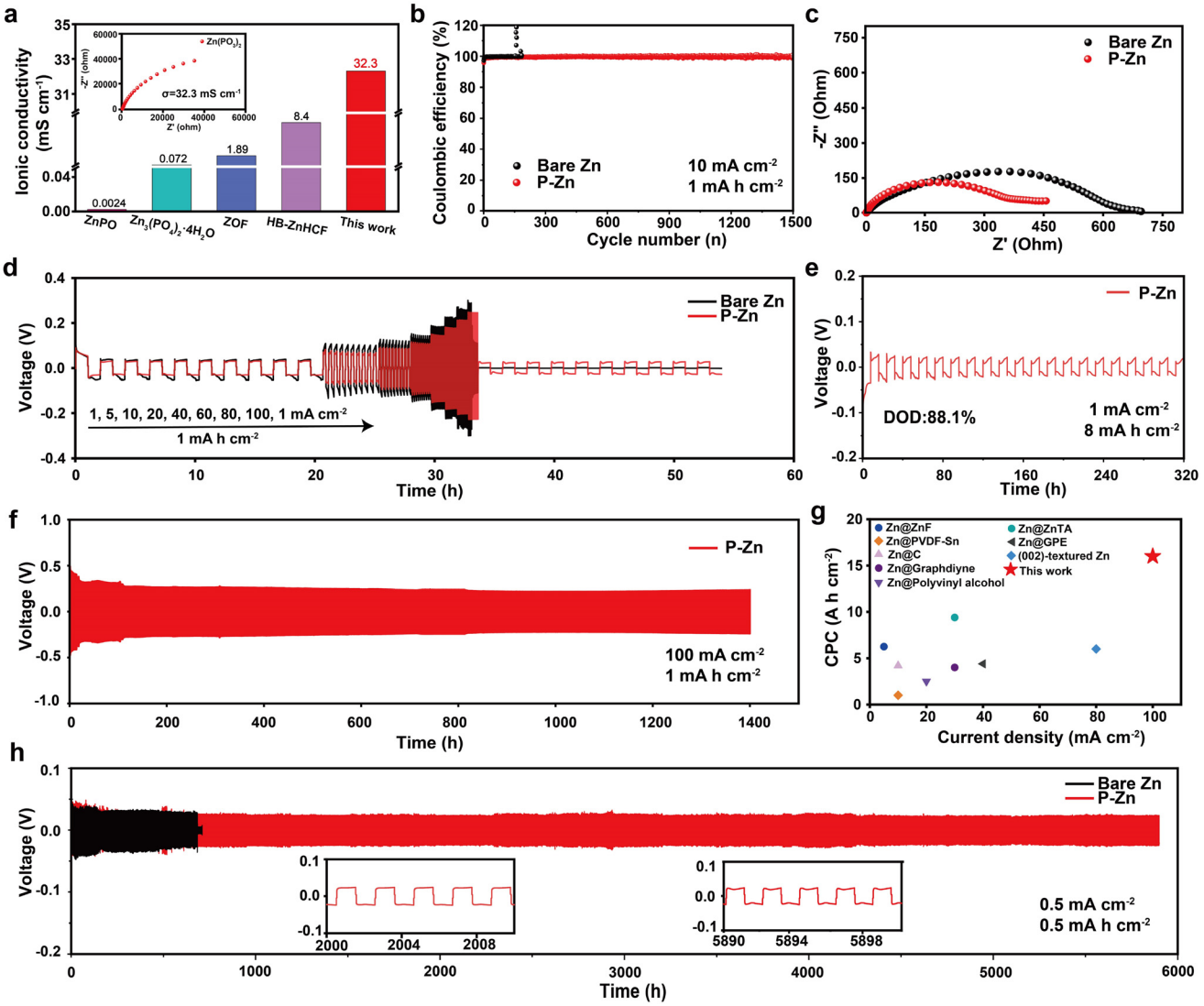

Fig. 2 (a) Comparison of the interphase with previous reports in terms of ionic conductivity; the inset shows the ionic conductivity of the $Zn(PO_3)_2$ interphase. (b) coulombic efficiencies of bare Zn||Cu and P–Zn||Cu cells. (c) Electrochemical impedance spectra of symmetric cells after 100 cycles. (d) Rate performances of bare Zn and P–Zn symmetric cells at various current densities. Cycling performance of the symmetric cells using bare Zn and P–Zn at (e) 1 mA cm^{-2} and 8 mAh cm^{-2}, (f) 100 mA cm^{-2} and 1 mAh cm^{-2}, and (h) 0.5 mA cm^{-2} and 0.5 mAh cm^{-2}. (g) Comparison of the symmetric cells with previous reports in terms of current density and cumulative capacity.

The results show that the P–Zn surface remains smooth even after 100 cycles (Fig. S16). Thus, the P–Zn layer effectively guides and stabilizes uniform Zn deposition, which is essential for achieving ultrahigh cycling stability. We also investigated the stability of the P–Zn interfacial layer after cycling. Symmetric P–Zn||P–Zn cells were disassembled after 5 cycles at a current density of 5 mA cm^{-2} for HAADF-STEM imaging and the corresponding elemental mapping analysis, as well as HRTEM and TOF-SIMS analyses. As shown in Fig. S17, the P–Zn interfacial layer maintains its structural integrity after cycling. Furthermore, the elemental mapping results confirm that Zn is uniformly deposited beneath the P–Zn interfacial layer, without inducing structural collapse or disruption of the protective layer. The HRTEM results of the interphase powder scraped from the surface of the cycled P–Zn reveal well-preserved lattice fringes of 0.281 and 0.298 nm, corresponding to the (130) and (−221) planes of $Zn(PO_3)_2$ (Fig. S18), confirming the preservation of the metaphosphate structure. Meanwhile, TOF-SIMS depth profiling shows dominant PO_3^- signals with negligible PO_4^{3-} species throughout sputtering (Fig. S19), indicating minimal hydrolysis or transition into orthophosphate phases. These observations suggest that the P–Zn layer effectively regulates Zn deposition and preserves interfacial stability during repeated plating/stripping cycles. Meanwhile, the diffraction peaks of $Zn_4SO_4(OH)_6{\cdot}5H_2O$ (ZHS) of cycled bare Zn can be clearly observed, indicating the occurrence of irreversible side reactions, which are absent in the cycled P–Zn samples (Fig. S20). As shown in Fig. 3j, the surface height difference of

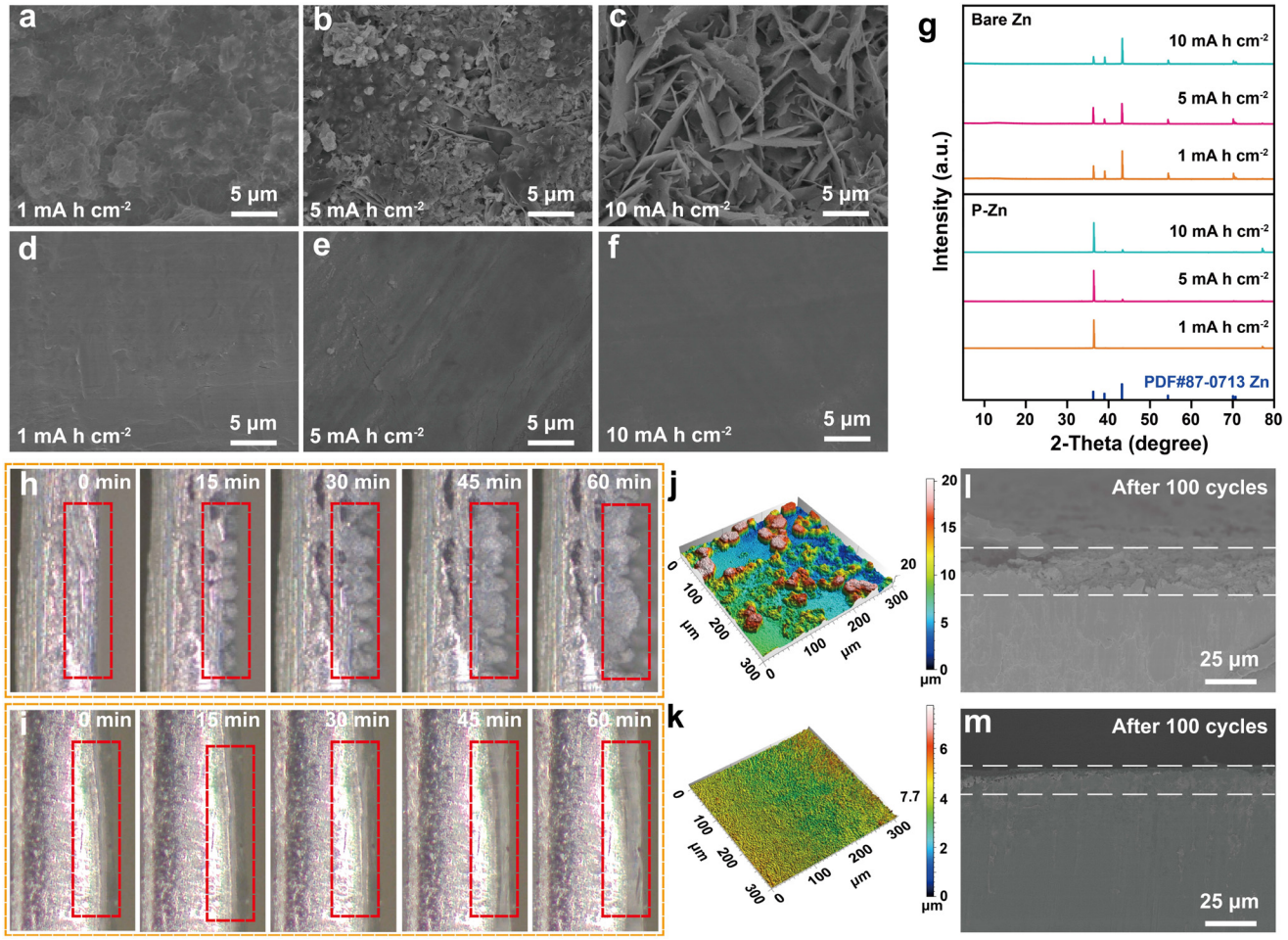

Fig. 3 Top-view SEM images of (a–c) bare Zn and (d–f) P–Zn electrodes after plating for 1, 5, and 10 mAh cm^{-2} at 1 mA cm^{-2}. (g) XRD patterns of bare Zn and P–Zn electrodes after plating for 1, 5, and 10 mAh cm^{-2} at 1 mA cm^{-2}. *In situ* optical microscopy observations of zinc deposition on (h) bare Zn and (i) P–Zn foil. Confocal laser scanning microscopy images of (j) bare Zn and (k) P–Zn electrodes after 100 cycles. Cross-sectional SEM images of (l) bare Zn and (m) P–Zn electrodes after 100 cycles at 1 mA cm^{-2} and 1 mAh cm^{-2}.

cycled bare zinc reaches 20 μm with visible pits, whereas the P–Zn electrode surface maintains a smooth surface (Fig. 3k). Furthermore, cross-sectional SEM images show significant differences in Zn deposition behavior between bare Zn and P–Zn anodes, given the denser and smoother morphology of deposited Zn in the P–Zn anode than in the bare Zn anode after cycling (Fig. 3l and m).

To further comprehend Zn diffusion behavior during deposition, chronoamperometry tests were conducted (Fig. S21). The lower current observed for P–Zn indicates a reduced 2D diffusion process because lateral Zn^{2+} diffusion is hindered, preventing dendrite growth. This phenomenon is attributed to the homogeneous nanoparticles in the $Zn(PO_3)_2$ interphase and its zincophilic property. Tafel curve measurements were performed to evaluate the corrosion resistance of the anodes. The presence of the $Zn(PO_3)_2$ interphase layer reduces the corrosion current from 0.59 mA cm^{-2} for bare Zn to 0.036 mA cm^{-2} for P–Zn (Fig. S22), indicating suppressed corrosion. This finding is attributed to the effective isolation of Zn from direct contact with the electrolyte by the $Zn(PO_3)_2$ layer. The effect of the P–Zn layer in inhibiting the hydrogen evolution reaction was also analyzed using a three-electrode system. The current density of the P–Zn electrode is always lower than that of bare Zn over the entire potential range (Fig. S23). Furthermore, symmetric cells were assembled and left to stand for 20 days to intuitively illustrate the effect of P–Zn layer in inhibiting parasitic reactions. Remarkably, the thickness of the symmetric cell with the bare Zn electrode increases from 3.23 mm to 3.81 mm, whereas the thickness of the P–Zn symmetric cell shows a minimal change from 3.23 mm to 3.25 mm (Fig. S24). These findings indicate significantly reduced corrosion and hydrogen evolution reactions.

DFT calculations were performed to determine the reason for the strong orientation of P–Zn along the (002) plane following the phosphating process. These calculations assess the interactions between the Zn (002), (100), and (101) planes with the $Zn(PO_3)_2$ interphase layer (Fig. 4a). The adsorption energies of the Zn (002), (101), and (100) crystal planes with the Zn $(PO_3)_2$ layer are −50.7, −43.8, and −3.9 eV, respectively (Fig. 4b). The significant interaction with the Zn (002) crystal

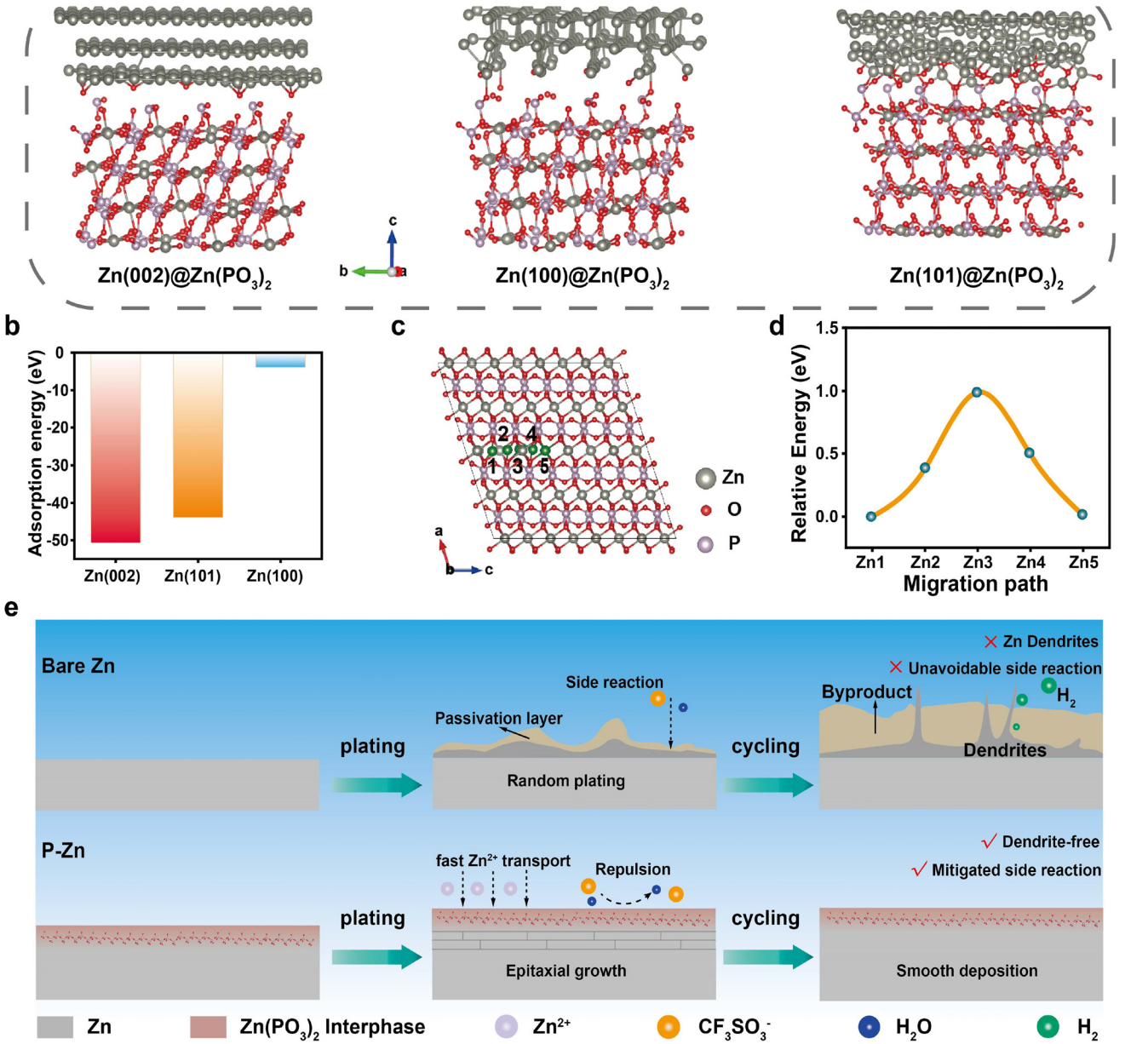

Fig. 4 (a) Adsorption models and (b) the corresponding adsorption energies of different Zn crystal facets with the $Zn(PO_3)_2$ interphase. (c) First-principles calculations and (d) migration energy barrier of the optimum Zn^{2+} diffusion pathway A in the $Zn(PO_3)_2$ interphase. (e) The schematic illustration of the Zn deposition/stripping behaviour on the bare Zn and P–Zn electrodes.

plane promotes the preferred orientation of the (002) crystal plane due to the synergistic effect of thermal radiation. Efficient Zn^{2+} transport within the interphase layer is crucial for the electrode's rate performance. An in-depth study of migration pathways and energy barriers of Zn^{2+} in the Zn $(PO_3)_2$ interphase layer was conducted to explore the cause of the outstanding electrochemical performance of the anode at high current densities (Fig. S25). Specifically, Zn^{2+} preferentially migrates along the c-axis of the $Zn(PO_3)_2$ crystal, encountering a minimum migration barrier of only 0.99 eV (Fig. 4c, d, Fig. S26 and 27), surpassing other fast Zn-ion conductors reported in the literature.[44,45] This highly efficient Zn^{2+} diffusion behavior ensures excellent high-rate performance and reversibility, leading to a dendrite-free Zn anode.

Based on the experimental findings above, a schematic summarizing the Zn deposition and stripping behavior on bare Zn and P–Zn electrodes is presented in Fig. 4e. Direct contact of Zn with the aqueous electrolyte on bare Zn leads to severe side reactions and irregular Zn deposition, ultimately resulting in dendritic growth. Conversely, the insulating nature of the Zn $(PO_3)_2$ interphase layer promotes Zn^{2+} deposition beneath it, thereby suppressing the corrosion and passivation of the Zn anode. The strong binding force between the P–Zn layer and the substrate accommodates the dynamic volume changes of the Zn

anode during cycling, preventing continuous electrolyte consumption. Fast zinc-ion transport, a low migration barrier, and short diffusion paths enable rapid zinc plating and stripping at high current densities on the Zn anode. The high orientation along the Zn (002) crystal plane facilitates ordered Zn epitaxial deposition, resulting in dense and dendrite-free Zn growth.

The effectiveness of the $Zn(PO_3)_2$ interphase layer in suppressing Zn dendrite formation and side reactions is demonstrated by the significantly enhanced long-term cycling stability of symmetric cells and the uniform Zn deposition. Additionally, aqueous Zn||$NH_4V_4O_{10}$ (NVO) and Zn||$K_{0.27}MnO_2{\cdot}0.54H_2O$ (KMO) full cells were assembled to comprehensively assess the practical applicability of the P–Zn anode in various cathode systems. The NVO nanorods were synthesized *via* a hydrothermal method and confirmed by XRD and SEM (Fig. S28). As illustrated in Fig. 5a, both bare Zn and P–Zn-based full cells show similar redox peaks in their CV profiles, indicating that the interfacial layer modification does not alter the fundamental electrochemical redox mechanism of the cathode material. However, the P–Zn||NVO cells exhibit superior rate capability and consistently higher specific capacities across a wide current density range (1.0–5.0 A g^{-1}), as shown in Fig. 5b. This performance enhancement indicates improved reaction kinetics and suppressed side reactions, as further supported by the reduced interfacial resistance observed in the EIS spectra at all states of charge (SOC) of 20%, 50%, and 70% (Fig. S29). Realistic aqueous zinc-ion batteries must consider key practical parameters such as the N/P ratio, active mass loading, and E/C ratio.[46] To validate the real-world applicability of the P–Zn design, full cells were further constructed under stringent practical conditions, including a thin zinc foil (20 μm), a high-mass-loading NVO cathode (12.5 mg cm^{-2}), a low N/P ratio of 1.8, and a low E/C ratio of 14.7 μL mAh^{-1}. Under these conditions, the P–Zn||NVO cell maintained stable cycling performance for 320 cycles with a high specific capacity of 161 mAh g^{-1} (Fig. 5c). Long-term cycling results further verify the stability of the interfacial design: at a current density of 2 A g^{-1} with an N/P ratio of 3.8, the cell delivered a specific capacity of 276 mAh g^{-1} and retained excellent capacity over 800 cycles (Fig. S30). Under high-rate conditions of 5 A g^{-1}, the P–Zn||NVO cell achieved a stable discharge capacity of 257 mAh g^{-1} over 1000 cycles (Fig. S31). Although AZIBs often suffer from poor cycling stability at low current densities due to intensified side reactions, the P–Zn||NVO cell still delivers significantly improved cycling performance compared to the Zn||NVO cell even at a low

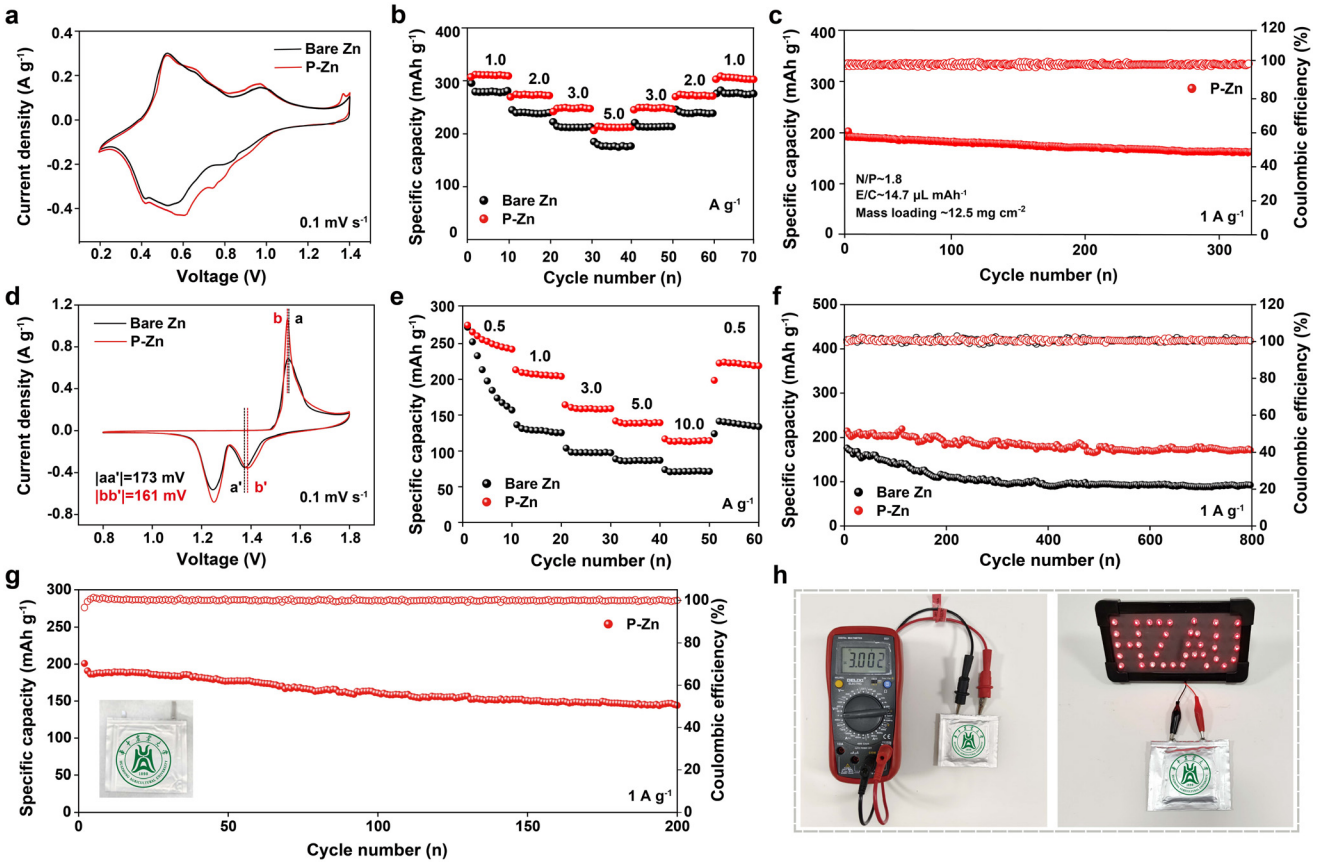

Fig. 5 (a) CV curves of Zn||NVO AZIBs at 0.1 mV s^{-1}. (b) Rate performances of the Zn||NVO AZIBs at various current densities. (c) Cycling performance at 1 A g^{-1} with a low N/P ratio of 1.8. (d) CV curves of Zn||KMO AZIBs at 0.1 mV s^{-1}. (e) Rate performances of the AZIBs at various current densities. (f) Cycling performance of the AZIBs at 1 A g^{-1}. (g) Cycling performance of the AZIB pouch cells at 1 A g^{-1}. (h) The illustration of laminated pouch cells.

current density of 30 mA g^{-1} (Fig. S32), underscoring the durability of the engineered interphase. In addition, $K_{0.27}MnO_2{\cdot}0.54H_2O$ cathode materials were synthesized *via* a facile sol–gel method, incorporating K^+ ions into MnO_2 nanoparticles to enhance structural stability and ion diffusion kinetics (Fig. S33). Pre-intercalated K^+ ions suppress Mn dissolution and help maintain structural integrity, making it an excellent zinc storage material. As shown in the SEM image, the diameter of KMO particles is approximately 100 nm. Bare Zn||KMO and P–Zn||KMO AZIBs exhibit similar redox peaks in the CV curves (Fig. 5d), and the improved reaction kinetics reduces the overpotential of the P–Zn||KMO full cell. Additionally, the larger integrated area under the CV curve suggests higher electrochemical activity for the P–Zn||KMO full cell, which is further supported by the lower interfacial resistance observed at all SOC levels of 20%, 50%, and 70% (Fig. S34). As shown in Fig. 5e, the P–Zn||KMO full cell performs better at different current densities. The specific capacity of the bare Zn||KMO full cell significantly decreases to 92 mAh g^{-1} with a capacity retention of 47% after 800 cycles at 1 A g^{-1}. Meanwhile, the P–Zn||KMO full cell exhibits significantly improved cycling performance even at a low current density of 30 mA g^{-1} (Fig. S35). Conversely, a high reversible capacity of 170 mAh g^{-1} can be obtained for P–Zn||KMO-based AZIBs after 800 cycles (Fig. 5f and Fig. S36). Pouch cells were assembled to further assess the practicality of the P–Zn anode. A 6 cm × 6 cm single-layer pouch cell was tested, and the results are shown in Fig. 5g. It has a specific capacity of 145 mAh g^{-1}, retaining approximately 72% of its capacity after 200 cycles at 1 A g^{-1}. Additionally, laminated pouch cells are successfully assembled alongside the single-layer configuration. Fig. 5h illustrates the practical application of the laminated pouch cell. When two single cells are connected in series, the pouch cell attains a voltage of 3 V. The laminated pouch cell can also reliably illuminate the light-emitting diode indicator of HZAU. The above findings demonstrate that P–Zn anodes hold the potential for wide-ranging applications due to their excellent electrochemical properties.

3 Conclusion

We present an *in situ* 40 nm thin highly conductive $Zn(PO_3)_2$ interphase layer with excellent zinc-ion transport properties, effectively combining zincophilic, hydrophilic, and insulative properties to produce a dendrite-free Zn anode. Due to its *in situ* growth strategy and the anionic substructure of metaphosphate chains, the P–Zn anode, featuring a thin $Zn(PO_3)_2$ interphase layer with a thickness of only 40 nm, demonstrates excellent stability and remarkable rate performance during cycling. Through visualization methods and theoretical calculations, the rooted homogeneous $Zn(PO_3)_2$ layer is confirmed to enhance the migration of Zn^{2+} ions and optimize Zn deposition, effectively mitigating Zn dendrite formation. Consequently, symmetric cells with P–Zn anodes exhibit remarkable cycling performance at an ultrahigh current density of 100 mA cm^{-2}, enduring over 16 000 cycles. Furthermore, they also demonstrate an exceptional cycle lifespan of 5900 h at 0.5 mA cm^{-2} and 0.5 mAh cm^{-2}. When assembled in full cells with NVO or KMO cathodes, the P–Zn anode delivers excellent electrochemical performance. The P–Zn||NVO cell achieves a high specific capacity of 276 mAh g^{-1} with 92.6% capacity retention over 800 cycles at 2 A g^{-1}. Even at a low N/P ratio of 1.8, the full cell maintains a high capacity of 161 mAh g^{-1} over 320 cycles. The P–Zn||KMO configuration also exhibits long-term cycling stability, retaining a capacity of 170 mAh g^{-1} over 800 cycles at 1 A g^{-1}. Additionally, the assembled pouch cell demonstrates promising durability, supporting the scalability of the approach. The comprehensive performance of the P–Zn anode is at an advanced level, showing high potential for the development of advanced Zn-based batteries with superior electrochemical performance.

Author contributions

F. C. and Y. L. supervised the research. J. W., Y. L., and D. H. conceived the project, analyzed the data, and wrote the manuscript. J. W., H. Q., K. Y., S. G., L. P., and P. Z. conducted the experiments and collected the data. D. X. gave helpful advice on manuscript preparation.

Conflicts of interest

The authors declare no competing financial interest.

Data availability

The data that support the findings of this study are available from the corresponding author upon reasonable request.

The Supplementary Information (SI) includes detailed experimental procedures, XRD patterns, XPS spectra, EIS spectra, AFM images, HAADF-STEM images, HRTEM images, SEM images, contact-angle measurements, and the electrochemical performance of the various samples. See DOI: https://doi.org/10.1039/d5eb00098j.

Acknowledgements

The research was financially supported by the National Natural Science Foundation Regional Innovation and Development Joint Fund (U23A20684), the National Natural Science Foundation of China (52272208, 52572226), and the Fundamental Research Funds for the Central Universities of China (2662025HXPY005, 2662025HXPY004). The authors gratefully acknowledge Prof. Congli Sun (Wuhan University of Technology) and Jiajing Wang (Wuhan University of Technology) for their assistance in obtaining high-quality HAADF-STEM images and EDS results that significantly supported the structural analysis in this work.

References

1 S. Gourley, R. Brown, B. Adams and D. Higgins, *Joule*, 2023, **7**, 1415–1436.
2 Y. Liu, X. Lu, F. Lai, T. Liu, P. Shearing, I. Parkin, G. He and D. Brett, *Joule*, 2021, **5**, 2845–2903.
3 Z. Zhu, T. Jiang, M. Ali, Y. Meng, Y. Jin, Y. Cui and W. Chen, *Chem. Rev.*, 2022, **122**, 16610–16715.
4 F. Li, D. Ma, K. Ouyang, M. Yang, J. Qiu, J. Feng, Y. Wang, H. Mi, S. Sun, L. Sun, C. He and P. Zhang, *Adv. Energy Mater.*, 2023, **13**, 2204365.
5 L. Ma, Q. Li, Y. Ying, F. Ma, S. Chen, Y. Li, H. Huang and C. Zhi, *Adv. Mater.*, 2021, **33**, e2007406.
6 F. Yang, J. Yuwono, J. Hao, J. Long, L. Yuan, Y. Wang, S. Liu, Y. Fan, S. Zhao, K. Davey and Z. Guo, *Adv. Mater.*, 2022, **34**, e2206754.
7 H. Jia, Z. Q. Wang, B. Tawiah, Y. D. Wang, C. Y. Chan, B. Fei and F. Pan, *Nano Energy*, 2020, **70**, 104523.
8 W. Lu, C. Zhang, H. Zhang and X. Li, *ACS Energy Lett.*, 2022, **6**, 2765.
9 B. Luo, Y. Wang, S. Zheng, L. Sun, G. Duan, J. Lu, J. Huang and Z. Ye, *Energy Storage Mater.*, 2022, **51**, 610–619.
10 C. Nie, G. Wang, D. Wang, M. Wang, X. Gao, Z. Bai, N. Wang, J. Yang, Z. Xing and S. Dou, *Adv. Energy Mater.*, 2023, **13**, 2300606.
11 F. Ling, L. Wang, F. Liu, M. Ma, S. Zhang, X. Rui, Y. Shao, Y. Yang, S. He, H. Pan, X. Wu, Y. Yao and Y. Yu, *Adv. Mater.*, 2023, **35**, e2208764.
12 J. Yang, S. Wang, L. Du, S. Bi, J. Zhu, L. Liu and Z. Niu, *Adv. Funct. Mater.*, 2024, **34**, 2314426.
13 N. Zhang, X. Chen, M. Yu, Z. Niu, F. Cheng and J. Chen, *Chem. Soc. Rev.*, 2020, **49**, 4203–4219.
14 X. Geng, X. Hou, X. He and H. Fan, *Adv. Energy Mater.*, 2024, **14**, 2304094.
15 H. Tian, J. Yang, Y. Deng, W. Tang, R. Liu, C. Xu, P. Han and H. Fan, *Adv. Energy Mater.*, 2022, **13**, 2202603.
16 F. Xie, H. Li, X. Wang, X. Zhi, D. Chao, K. Davey and S. Qiao, *Adv. Energy Mater.*, 2021, **11**, 2003419.
17 H. Cai, S. Bi, R. Wang, L. Liu and Z. Niu, *Angew. Chem., Int. Ed.*, 2021, **61**, e202205472.
18 Z. Chen, T. Wang, Y. Hou, Y. Wang, Z. Huang, H. Cui, J. Fan, Z. Pei and C. Zhi, *Adv. Mater.*, 2022, **34**, e2207682.
19 Q. Li, H. Hong, J. Zhu, Z. Wu, C. Li, D. Wang, P. Li, Y. Zhao, Y. Hou, G. Liang, F. Mo, H. Cui and C. Zhi, *ACS Nano*, 2023, **17**, 23805–23813.
20 Y. Su, B. Chen, Y. Sun, Z. Xue, Y. Zou, D. Yang, L. Sun, X. Yang, C. Li, Y. Yang, X. Song, W. Guo, S. Dou, D. Chao, Z. Liu and J. Sun, *Adv. Mater.*, 2023, **35**, e2301410.
21 J. Zheng, Y. Deng, J. Yin, T. Tang, R. Garcia-Mendez, Q. Zhao and L. Archer, *Adv. Mater.*, 2022, **34**, e2106867.
22 Z. Chen, Q. Wu, X. Han, C. Wang, J. Chen, T. Hu, Q. He, X. Zhu, D. Yuan, J. Chen, Y. Zhang, L. Yang, Y. Ma and J. Zhao, *Angew. Chem., Int. Ed.*, 2024, **63**, e202401507.
23 X. He, Y. Cui, Y. Qian, Y. Wu, H. Ling, H. Zhang, X. Kong, Y. Zhao, M. Xue, L. Jiang and L. Wen, *J. Am. Chem. Soc.*, 2022, **144**, 11168–11177.
24 S. Pu, C. Gong, Y. Tang, Z. Ning, J. Liu, S. Zhang, Y. Yuan, D. Melvin, S. Yang, L. Pi, J. Marie, B. Hu, M. Jenkins, Z. Li, B. Liu, S. Tsang, T. Marrow, R. Reed, X. Gao, P. Bruce and A. Robertson, *Adv. Mater.*, 2022, **34**, e2202552.
25 W. Wang, G. Huang, Y. Wang, Z. Cao, L. Cavallo, M. Hedhili and H. Alshareef, *Adv. Energy Mater.*, 2022, **12**, 2102797.
26 L. Cao, D. Li and T. Pollard, *Nat. Nanotechnol.*, 2021, **16**, 902–910.
27 S. S. Shinde, J. Y. Jung and N. K. Wagh, *Nat. Energy*, 2021, **6**, 592–604.
28 J. Li, Z. Zheng, Z. Yu, F. She, L. Lai, J. Prabowo, W. Lv, L. Wei and Y. Chen, *J. Mater. Chem. A*, 2023, **11**, 3051–3059.
29 S. Zhang, M. Ye, Y. Zhang, Y. Tang, X. Liu and C. Li, *Adv. Funct. Mater.*, 2023, **33**, 2208230.
30 G. Han, A. Vasylenko, A. Neale, B. Duff, R. Chen, M. Dyer, Y. Dang, L. Daniels, M. Zanella, C. Robertson, L. Kershaw Cook, A. Hansen, M. Knapp, L. Hardwick, F. Blanc, J. Claridge and M. Rosseinsky, *J. Am. Chem. Soc.*, 2021, **143**, 18216–18232.
31 Z. Zheng, S. Guo, M. Yan, Y. Luo and F. Cao, *Adv. Mater.*, 2023, **35**, 2304667.
32 C. F. Holder and R. E. Schaak, *Nanoscale Mater.*, 2019, **13**, 7359.
33 H. Xie, M. Hong, E. M. Hitz, X. Wang, M. Cui, D. J. Kline, M. R. Zachariah and L. Hu, *J. Am. Chem. Soc.*, 2020, **142**, 17364–17371.
34 S. Zhao, Y. Zhang, J. Li, L. Qi, Y. Tang, J. Zhu, J. Zhi and F. Huang, *Adv. Mater.*, 2023, **35**, e2300195.
35 C. Cui, D. Han, H. Lu, Z. Li, K. Zhang, B. Zhang, X. Guo, R. Sun, X. Ye, J. Gao, Y. Liu, Y. Guo, R. Meng, C. Wei, L. Yin, F. Kang, Z. Weng and Q. Yang, *Adv. Energy Mater.*, 2023, **13**, 2301466.
36 M. Liu, W. Yuan, G. Ma, K. Qiu, X. Nie, Y. Liu, S. Shen and N. Zhang, *Angew. Chem., Int. Ed.*, 2023, **62**, e202304444.
37 Q. Cao, Y. Gao, J. Pu, X. Zhao, Y. Wang, J. Chen and C. Guan, *Nat. Commun.*, 2023, **14**, 641.
38 Q. Hu, J. Hou, Y. Liu, L. Li, Q. Ran, J. Mao, X. Liu, J. Zhao and H. Pang, *Adv. Mater.*, 2023, **35**, e2303336.
39 Z. Hu, F. Zhang, Y. Zhao, H. Wang, Y. Huang, F. Wu, R. Chen and L. Li, *Adv. Mater.*, 2022, **34**, e2203104.
40 X. Luan, L. Qi, Z. Zheng, Y. Gao, Y. Xue and Y. Li, *Angew. Chem., Int. Ed.*, 2023, **62**, e202215968.
41 P. Zhang, Z. Wu, S. Zhang, L. Liu, Y. Tian, Y. Dou, Z. Lin and S. Zhang, *Nano Energy*, 2022, **102**, 107721.
42 Y. Qin, H. Li, C. Han, F. Mo and X. Wang, *Adv. Mater.*, 2022, **34**, e2207118.
43 K. Zhu, C. Guo, W. Gong, Q. Xiao, Y. Yao, K. Davey, Q. Wang, J. Mao, P. Xue and Z. Guo, *Energy Environ. Sci.*, 2023, **16**, 3612–3622.
44 X. Zeng, J. Mao, J. Hao, J. Liu, S. Liu, Z. Wang, Y. Wang, S. Zhang, T. Zheng, J. Liu, P. Rao and Z. Guo, *Adv. Mater.*, 2021, **33**, 2007416.
45 L. Hong, X. Wu, Y. Liu, C. Yu, Y. Liu, K. Sun, C. Shen, W. Huang, Y. Zhou, J. Chen and K. Wang, *Adv. Funct. Mater.*, 2023, **33**, 2300952.
46 S. S. Shinde, N. K. Wagh, C. H. Lee, D. H. Kim, S. H. U. Lee and J. H. Lee, *Adv. Mater.*, 2023, **35**, 2303509.